First-principles study of electronic and optical properties of two-dimensional Ca$_2$N electride using pseudoatomic orbital basis set

Jinwoong Chae and Gunn Kim[*]

Department of Physics and HMC, Sejong University, Seoul 05006, Republic of Korea

Dicalcium nitride (Ca$_2$N) is a two-dimensional (2D) electride with unique electronic behavior. In this study, we use pseudoatomic orbital (PAO) basis sets to investigate its electronic and optical properties. This methodology provides an accurate representation of the electronic structure associated with the interlayer and surface anionic states of the Ca$_2$N bilayer, enabling a comprehensive study of its optical properties. We identify several peaks in the dielectric functions which correspond to interband transitions. Our analysis of the optical conductivity and linear optical spectra, derived from these dielectric functions, reveals distinct peaks in the linear optical spectra of both bulk and bilayer Ca$_2$N. These peaks are influenced by the in-plane and out-of-plane vectors. This investigation provides valuable insights into the interband transitions and optical behavior of this intriguing 2D electride. It also lays the foundation for future studies of promising 2D electrides.

I. INTRODUCTION

Electrides are a fascinating class of materials with unique electronic and physical properties [1,2]. These materials contain electrons occupying interstitial spaces in positively charged frameworks, which gives them the unusual property of having electrons acting as anions [3–14]. This property, known as interstitial anionic electron (IAE) behavior, endows electrides with a range of remarkable properties, including low work functions, resistivity anisotropy, metal-insulator and metal-semiconductor transitions, and even superconductivity.

Electrides have attracted increasing attention in recent years due to their potential for applications in electronics, energy storage, and catalysis. However, the synthesis of stable electrides has historically been challenging [15–20]. A turning point in this field was the successful synthesis of Ca$_{12}$Al$_{14}$O$_{33}$, an electride with exceptional thermodynamic and chemical stability. This development has opened new opportunities for investigating the exotic properties of electrides and for their practical application [15–20].

The research landscape for electrides has broadened in recent years to include two-dimensional (2D) materials [6]. The materials exhibit a layered structure analogous to graphite and have sparked considerable interest in the scientific community. Like their three-dimensional counterparts, 2D electrides contain IAEs, but they are confined to interlayer spaces. This is similar to a spread sandwiched between two slices of bread. The study of 2D electrides, such as Y$_2$C, Gd$_2$C, Sc$_2$C, and Al$_2$C, has unveiled their intriguing properties [21–23]. These materials have shown promise for applications in electronics, energy storage, and catalysis.

These 2D electrides, characterized by IAE states near the Fermi level, exhibit a variety of fascinating properties. Compounds such as Ca$_2$N, Y$_2$C, and Gd$_2$C exhibit intriguing metallic properties, with Gd$_2$C even showing ferromagnetic behavior [24–27]. This suggests the potential richness of their electronic and optical nature and warrants further exploration.

In this study, we overcome the limitations of pseudoatomic orbital (PAO) basis sets by presenting a methodology to yield reliable results in density functional theory (DFT) calculations for 2D electrides. We explore the electronic and optical properties of bulk and bilayer Ca$_2$N, leveraging both PAO and plane-wave (PW) basis sets in our DFT calculations.

We perform a comparative analysis of the band structures calculated with these two basis sets and determine the dielectric functions derived from the band structures. This allows us to identify specific peaks in the dielectric functions that are indicative of interband transitions. We then examine the optical conductivity and linear optical spectra obtained from the dielectric functions of bulk Ca$_2$N, enriching our understanding of its optical behavior. Our investigation reveals that the linear optical spectra of bulk Ca$_2$N exhibit distinct peaks for in-plane and out-of-plane vectors. This is in contrast to previous research on Ca$_2$N, which focused primarily on its plasmonic properties and attenuation coefficient [28–30]. Our results extend this understanding by investigating the interband transition and optical properties of Ca$_2$N.

II. COMPUTATIONAL DETAILS

We used DFT to explore the electronic and optical properties of bulk and bilayer Ca$_2$N structures. We performed the calculations using two different codes: the OPENMX code [31] and the Vienna *Ab initio* Simulation Package (VASP) [32,33].

For the OPENMX code, we adopted a PAO basis set to describe the electronic charge density and used the norm-conserving method to represent the interactions between electrons and ions [34,35]. We used the Perdew-Burke-Ernzerhof (PBE) type generalized gradient approximation
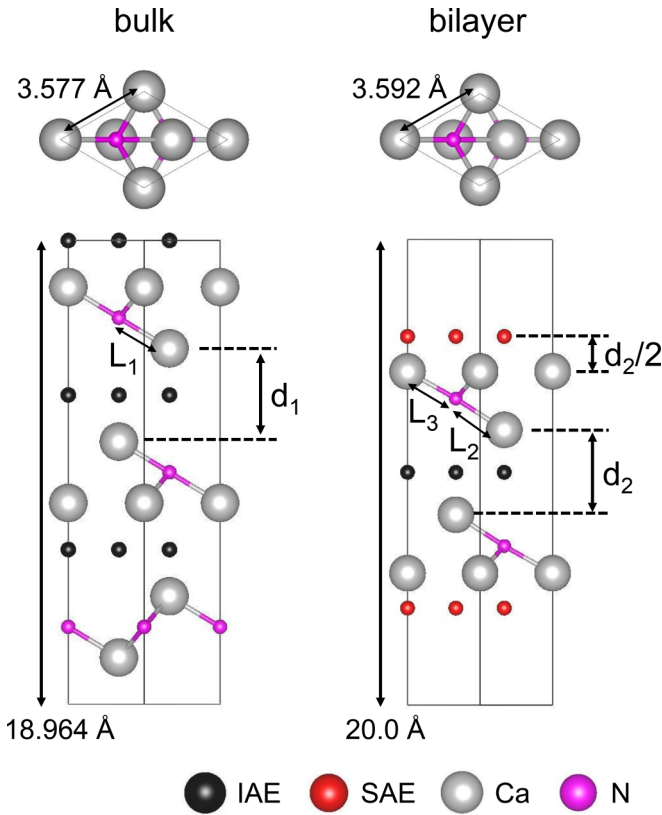
*Corresponding author: gunnkim@sejong.ac.kr

FIG. 1. Optimized bulk and bilayer Ca_2N structures. L_1 represents the distance between calcium and nitrogen atoms in bulk. Meanwhile, L_2 and L_3 represent the distance between nitrogen atoms and calcium atoms on the surface or close to the interlayer region, respectively, in the bilayer.

(GGA) functional to model the exchange-correlation energy.

On the other hand, for the VASP code, we applied a PW basis set to describe the electronic charge density and used the projector augmented-wave method to describe the interactions between electrons and ions [36,37]. We also used the PBE-type GGA functional to model the exchange-correlation energy [38]. To account for van der Waals interactions, we used Grimme's DFT-D3 (a dispersion correction for DFT calculations) method [39].

The kinetic energy cutoff was set at 300 Ry and 800 eV for the OPENMX and VASP codes, respectively. The convergence tolerance was set to 10^{-8} hartree energy for the OPENMX code and 10^{-6} eV for the VASP code. We used a Γ-centered $18 \times 18 \times 6$ ($18 \times 18 \times 1$) k-point grid for the electronic structure calculations in bulk (bilayer) Ca_2N. Finally, we used the VESTA and GNUPLOT packages to visualize the model structures and plot the band structures, density of states, and optical properties.

III. RESULTS AND DISCUSSION

A. Optimized structures

First, we obtained the optimized structures of bulk and bilayer Ca_2N using plane-wave basis sets. The optimized structures are shown in Fig. 1. The gray circles represent cal-

cium atoms, and the magenta circles represent nitrogen atoms. The lattice parameters of bulk (bilayer) Ca_2N are $a = 3.577$ (3.592) Å and $c = 18.964$ (20.000) Å.

In the bulk Ca_2N structure, the bond length between the Ca and N atoms L_1 is 2.416 Å. In the bilayer, the periodicity is lost in the c-axis direction, which breaks the symmetry and leads to structural changes. Therefore, the Ca_2N bilayer has two different bond lengths, L_2 and L_3. L_2 represents the bond length between the Ca atom near the interlayer and the N atom, and L_3 represents the bond length between the outermost Ca atom and the N atom. Bond lengths L_2 and L_3 are 2.472 and 2.380 Å, respectively. L_3 is about 0.1 Å shorter than L_2 due to the outermost Ca atom's contact with the vacuum layer. The interlayer distances d_1 and d_2 are 3.812 and 3.650 Å, respectively. We placed dummy atoms in the middle of the interlayer, as indicated by black circles in Fig. 1. We also introduced dummy atoms (red circles in Fig. 1) to simulate the anionic electrons on the surface of the Ca_2N bilayer because few-layer electrides are known to have anionic electrons at their surface.

Dummy atoms, which have no nuclear charge and only a basis function, are widely used in quantum chemistry and condensed matter physics calculations. They allow the calculation of electron densities in regions without real atoms, effectively determining the charge distribution in vacancy regions. Previous studies emphasized the importance of including these anionic electrons at the surface and in the interlayer space for accurate predictions of electride material properties [28,40].

B. Electronic properties of Ca_2N bulk and bilayer

We examined the electronic band structures of bulk and bilayer Ca_2N using the PW basis set to understand the importance of IAE states within positively charged frameworks and their effects on the electronic properties of electrides. To compare the band structures obtained using different basis sets (PAO and PW), we present the results in Fig. 2(a), with the black (red) lines representing calculations using the PW (PAO) basis sets. In addition, we investigated whether the band structure of bulk Ca_2N without dummy atoms, even with PAO basis sets, could describe the IAE states well. Unfortunately, the band lines obtained from PAO basis sets did not align well with the $+2$ eV energy level at the Γ-K and Γ-M paths compared to those from the PW basis sets. To emphasize this discrepancy, we indicate the band line exhibiting the difference between PAO and PW basis sets with blue arrows in Fig. 2(a). As a result, although the cutoff radii of the PAOs effectively include the interlayer region for Ca atoms, their application solely in positively charged frameworks does not accurately depict the IAE states.

To address the discrepancy between the band structures calculated with PAO and PW basis sets, we introduced dummy atoms at the IAE sites in the middle of the interlayer region. The cutoff radius of the PAOs in these dummy atoms was set to $9.0a_0$, where a_0 is the Bohr radius, which is the same as the cutoff radius of the PAO basis sets in Ca atoms. This resulted in a band structure that was more comparable to that obtained with PW basis sets. However, it has been raised that the dummy atoms at the surface anionic electron (SAE) sites may not necessarily need to have the same cutoff radius as the IAE sites. To investigate this, we calculated the band structure
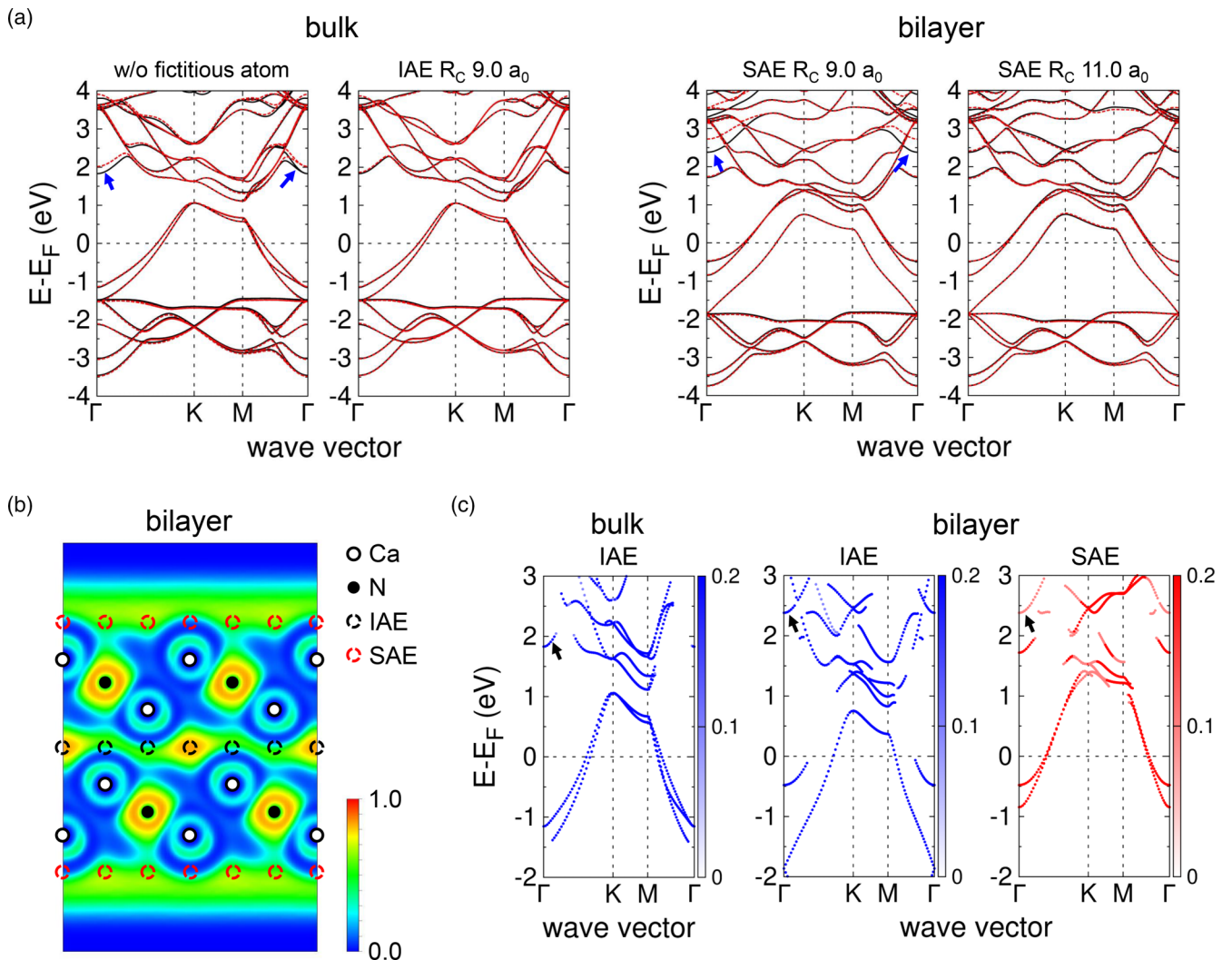
FIG. 2. (a) The band structures of bulk and bilayer Ca_2N with black (red) band lines representing the results obtained using the PW (PAO) basis set. The cutoff radius R_c of the PAO basis sets in dummy atoms is measured in a_0, which is the Bohr radius, equivalent to 0.529 Å. (b) Electron localization function (ELF) plots of bilayer Ca_2N with the Ca (N) atoms indicated by black lined (filled) circles and the IAE (SAE) sites represented by black (red) dashed circles. (c) The s-orbital band of the IAE and SAE states are shown by the blue and red dashed lines, respectively, in the orbital-projected band structure plots of the IAE and SAE.

of bilayer Ca_2N using PAO basis sets, including dummy atoms at the SAE sites with a cutoff radius of $9.0a_0$. However, the resulting band structure still did not agree with that derived from the PW basis set along the Γ-K and Γ-M paths. At the Γ point, the band obtained with PW basis sets has a band minimum of $+2.4$ eV, while the band obtained with PAO basis sets goes higher and has a band minimum of $+2.7$ eV. This suggests that the cutoff radius of the dummy atoms at the SAE sites may need to be larger than that of the IAE sites in order to obtain a band structure that is in agreement with that obtained with PW basis sets. Further investigation is needed to determine the optimal cutoff radius for the dummy atoms at the SAE sites.

To further investigate the systems, we generated an electron localization function (ELF) plot of the bilayer Ca_2N, which gives us a clear view of the electron density distribution at the surface. As shown in Fig. 2(b), the ELF plot shows the delocalized distribution of anionic electrons at the surface,

similar to a 2D electron gas. The black lined (filled) circles indicate the Ca (N) atoms, while the black (red) dashed circles represent the IAE (SAE) sites. The delocalized distributions of SAEs suggest that the cutoff radius of the PAO basis sets in the surface dummy atoms is greater than $9.0a_0$. We found that by adjusting the cutoff radius of the dummy atom at the SAE site to $11.0a_0$ and keeping the cutoff radius of the PAO basis set in the dummy atom at the IAE site at $9.0a_0$, we were able to obtain a band structure of the bilayer Ca_2N that is comparable to the results obtained using the PW basis set. Therefore, to accurately calculate the band structure of bilayer Ca_2N when dummy atoms are placed at the SAE sites, the cutoff radius of the PAO basis set should be set longer in the region with SAE than in the region with IAE, as shown in Fig. 1.

Next, we studied the band line mismatch between PAO and PW basis sets in the computation of the orbital-projected band structures of bulk and bilayer Ca_2N to figure out the reason. Our analysis suggests that the discrepancy occurs due to the
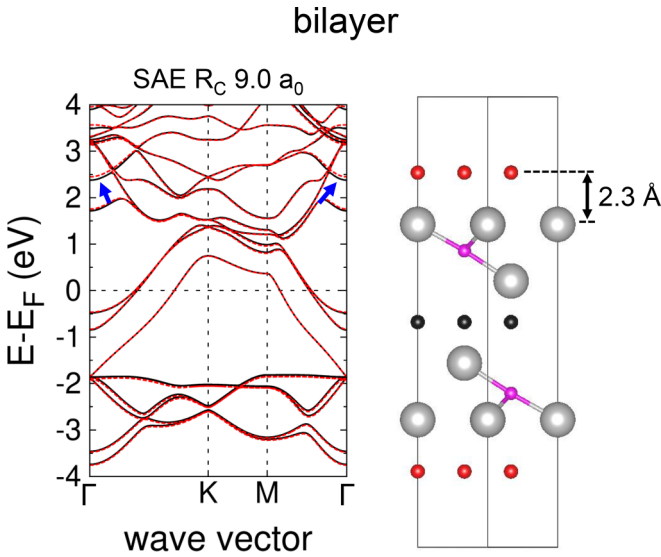
FIG. 3. Band structure of the Ca_2N bilayer with the dummy atom positioned 2.3 Å above the surface.

inadequate description of SAE by the PAO basis with a shorter cutoff radius. To gain better insight into this, we present the orbital projection plot of the band structure of bulk and bilayer Ca_2N in Fig. 2(c). This plot shows that the s-orbital bands are related to the IAE and SAE states. As indicated by the black arrows with $+2.0$ ($+2.4$) eV in the bulk (bilayer) in Fig. 2(c), the electronic structures calculated using the PAO and PW basis sets have mismatched band lines, which arise due to the contributions from the sparse IAE and SAE states. Therefore, it is crucial to establish the appropriate cutoff radius of the PAO basis sets at the IAE and SAE sites in the dummy atoms to ensure an accurate calculation of 2D electrides with PAO basis sets.

The electronic band structure of a surface can be accurately represented by placing dummy atoms with zero potential and only localized orbitals. In previous calculations, we used a longer cutoff radius ($11.0a_0$) to achieve the same electronic structure as the plane-wave calculation. However, we found that repositioning the dummy atom farther from its previous location resulted in an electronic structure nearly identical to that obtained with plane-wave calculations. Specifically, placing the dummy atom 2.3 Å away from the surface Ca atom resulted in a band structure that is in good agreement with the plane-wave calculation. We present the model and the electronic band structures in Fig. 3. In this calculation, the cutoff radius for the dummy atoms was set to $9.0a_0$. In summary, by setting the cutoff distance of the dummy atom to $9.0a_0$, we observed that the electronic band structure with the dummy atom positioned at 2.3 Å from the Ca_2N outer surface (as shown in Fig. 3) is more consistent with the results of the plane-wave calculations. This is in contrast to the band structure with the dummy atom at a distance of 1.825 Å (shown in Fig. 2), which exhibits a more significant deviation.

C. Optical properties of Ca_2N bulk and bilayer

To accurately represent the electronic structures of the Ca_2N bulk and bilayer, we used PAO basis sets and incorpo-

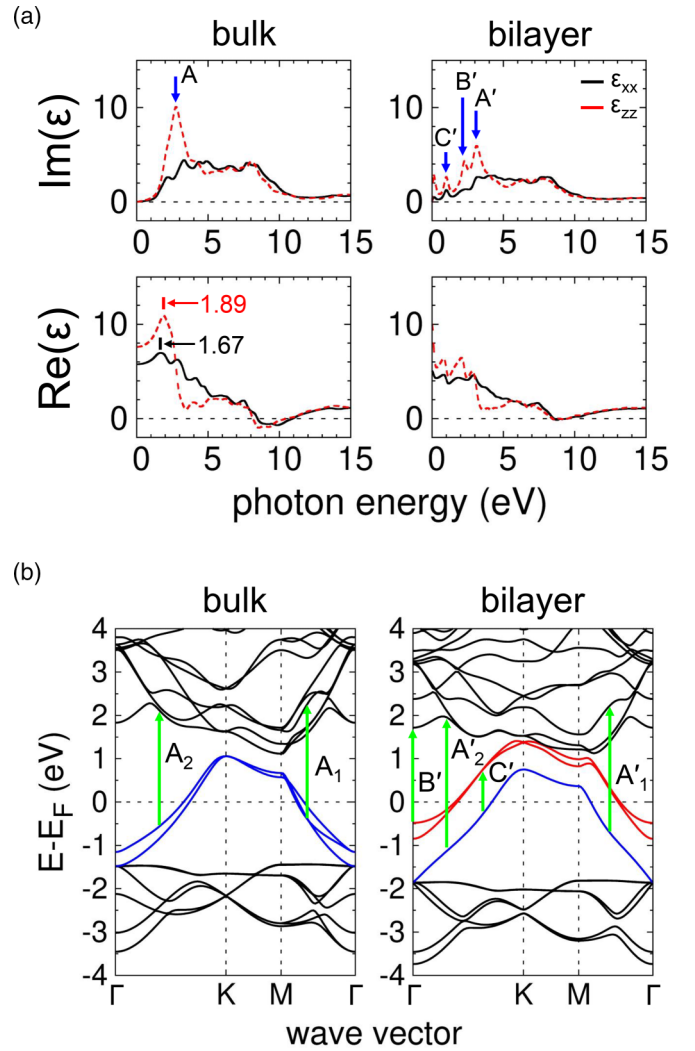FIG. 4. (a) The dielectric functions of bulk and bilayer Ca_2N. The black (red) lines indicate the dielectric functions perpendicular (parallel) to the c axis. (b) The electronic band structures of the Ca_2N bulk and bilayer.

rated dummy atoms with determined PAO cutoff radii. With these parameters established, our focus shifted to the analysis of the optical properties of both configurations. For this purpose, we calculated the dielectric functions of bulk and bilayer Ca_2N, obtaining results consistent with previous studies using PW basis sets [28]. The dielectric functions, shown in Fig. 4(a), were calculated using the Kubo-Greenwood formula from the OPENMX package. The complex dielectric function $\varepsilon(\omega)$ is defined as follows:

$$\varepsilon(\omega) = \mathrm{Re}[\varepsilon(\omega)] + i\mathrm{Im}[\varepsilon(\omega)], \qquad (1)$$

where $\mathrm{Re}[\varepsilon(\omega)]$ and $\mathrm{Im}[\varepsilon(\omega)]$ denote the real and imaginary parts of the dielectric function, respectively. The diagonal elements of the dielectric tensor $\varepsilon_{ij}(\omega)$ are represented by the dielectric functions $\varepsilon_{xx}(\omega)$ and $\varepsilon_{zz}(\omega)$. The hexagonal symmetry results in $\varepsilon_{xx}(\omega)$ and $\varepsilon_{yy}(\omega)$ are identical. While $\varepsilon_{xx}(\omega)$ is oriented perpendicular to the c axis, $\varepsilon_{zz}(\omega)$ runs parallel to it.

Our study reveals that the dielectric properties of bulk and bilayer Ca_2N exhibit anisotropic behavior relative to the z

axis when the photon energy is below +6.0 eV. However, above this energy threshold, the properties become isotropic. In terms of the dielectric functions $\varepsilon_{xx}(\omega)$ and $\varepsilon_{zz}(\omega)$, no notable peaks are present in $\varepsilon_{xx}(\omega)$, whereas $\varepsilon_{zz}(\omega)$ displays a few prominent peaks. The high-energy range above +9.0 eV also exhibits characteristics resembling the Drude model. In Fig. 4(a), we observe that the imaginary part of the dielectric function for bulk Ca_2N displays a single peak labeled as A, while the dielectric function for bilayer Ca_2N exhibits three peaks designated as A′, B′, and C′. Peak A has a photon energy of 2.75 eV, whereas peaks A′, B′, and C′ have energies of 3.12, 2.27, and 1.00 eV, respectively. We have identified energy ranges in the electronic band structures that explain the interband transitions responsible for these dielectric function peaks. These transitions are represented by green arrows in Fig. 4(b). Figure 4(b) presents the electronic band structures of both bulk and bilayer Ca_2N. The blue lines depict the bands associated with IAE states, while the red lines in the band structure plot of the Ca_2N bilayer represent the SAE states. Notably, the flat band lines observed at −1.5 (−1.9) eV in bulk (bilayer) correspond to the strongly localized N $2p$ orbitals.

To study the interband transitions in Ca_2N, we examined the energy difference between the valence and conduction bands as a function of photon energy, corresponding to the peak position of the imaginary part of the dielectric functions. The flat bands at −1.5 (−1.9) eV in the electronic band structure of bulk (bilayer) Ca_2N hardly contribute to the interband transition, which are localized states originating mainly from the N atoms. Therefore, peak A of the dielectric function of bulk Ca_2N predominantly represents the interband transition originating from the valence band of the IAE states. Specifically, the interband transition from the valence band of the IAE states could occur in two possible cases, namely, A_1 and A_2 (A_1' and A_2'), as shown in Fig. 4(b) for the bulk (bilayer) Ca_2N. The A_1 (A_1') interband transition of bulk (bilayer) Ca_2N indicates the transition between the valence band of the IAE states and the conduction band of the IAE states, with the corresponding band lines located in the Γ-M path near +2.0 eV in Fig. 2(c). On the other hand, the A_2 (A_2') interband transition of bulk (bilayer) Ca_2N represents the transition between the valence band of the IAE states and the conduction band of the Ca $3d$ orbital states in the Γ-K path.

For the bilayer, the peak at 0 eV in the dielectric function is due to the transition between the bands of two SAE states. This transition is also observed in the Ca_2N monolayer [28]. The bilayer Ca_2N exhibits peaks B′ and C′ in the imaginary part of the dielectric function, which are absent in bulk Ca_2N. Peak B′ corresponds to the interband transition between the valance band of the SAE states and the conduction band of the Ca $3d$ orbital. The SAE states are typically observed in few-layer structures of 2D electrides. Therefore, the interband transition between the valence band of the SAE states and the conduction band of the Ca $3d$ orbital is observed in only few-layer structures of Ca_2N, such as mono-, bi-, and trilayers. We also observed the interband transition between the IAE and SAE bands in the imaginary part of the dielectric function. The peak C′ of the bilayer Ca_2N corresponds to the difference in energy level between the valance band of the IAE states and the conduction band of the SAE states. Peak C′ represents the

TABLE I. The transition dipole moments (TDMs) for the interband transitions A_1, A_2, A_1', A_2', B′, and C′. The notation P^2 is used to represent the square of the TDM, which is expressed in units of square debyes.

	A_1	A_2	A_1'	A_2'	B′	C′
P^2	41.94	35.56	20.00	37.21	181.38	21.59

interband transition from the valance band of the IAE states to the conduction band of the SAE states. Therefore, even with PAO basis sets, we can explain the interband transitions of the dielectric function by accurately describing the IAE and SAE states in the band structure.

We have calculated the transition dipole moment (TDM) for both bulk and bilayer Ca_2N using VASP. The squares of the TDM are proportional to the transition probabilities between the valence and conduction bands. The squares of the TDM are tabulated in Table I. The results confirm the interband transition probabilities for both structures.

Next, we move on to investigate the linear optical properties of bulk Ca_2N by calculating its optical conductivity from the dielectric function. The optical conductivity $\sigma(\omega)$ is related to the complex dielectric function. In the OPENMX package, the dielectric function is computed in terms of the relative permittivity ε_r. The optical conductivity is then calculated as follows:

$$\sigma(\omega) = i[1 - \varepsilon_r(\omega)]\varepsilon_0 \omega, \qquad (2)$$

where ε_0 and ω are the permittivity of vacuum and the frequency of the incident wave, respectively. The real and imaginary parts of the optical conductivity $\sigma(\omega)$ are related to the real and imaginary parts of the dielectric function $\varepsilon(\omega)$. We plot the optical conductivity of bulk Ca_2N in Fig. 5(a), where the black and red lines represent the real and imaginary parts of $\sigma(\omega)$, respectively. The real part of $\sigma(\omega)$ shows peaks at 8.40 and 8.05 eV for σ_{xx} and σ_{zz}, respectively. The secondary peak at 2.79 eV in σ_{zz} corresponds to peak A in the dielectric function. The dip position between 11 and 13 eV in $\sigma(\omega)$ is due to the Drude-like characteristic of the dielectric function at high photon energies. Our results provide insight into the linear optical properties of bulk Ca_2N. The peaks in the real part of $\sigma(\omega)$ indicate the presence of electronic transitions in the material. The Drude-like characteristic of the dielectric function at high photon energies suggests that bulk Ca_2N is a good conductor of electricity. These results may be useful for future studies of bulk Ca_2N, such as investigating its potential applications in optoelectronics and photovoltaics.

The optical spectra of bulk Ca_2N were investigated using UV-visible spectroscopy [41–43]. The results provide valuable insights into the optoelectronic properties of this material. The linear optical spectra of bulk Ca_2N can be calculated from the optical conductivity $\sigma(\omega)$, which is obtained from the dielectric function. The formulas are as follows [44]:

$$\alpha(\omega) = \frac{\sqrt{2}\omega}{c}[\sqrt{\mathrm{Re}(\varepsilon)^2 + \mathrm{Im}(\varepsilon)^2} - \mathrm{Re}(\varepsilon)]^{\frac{1}{2}}, \qquad (3)$$

$$k(\omega) = \left(\frac{\sqrt{\mathrm{Re}(\varepsilon)^2 + \mathrm{Im}(\varepsilon)^2} - \mathrm{Re}(\varepsilon)}{2}\right)^{\frac{1}{2}}, \qquad (4)$$
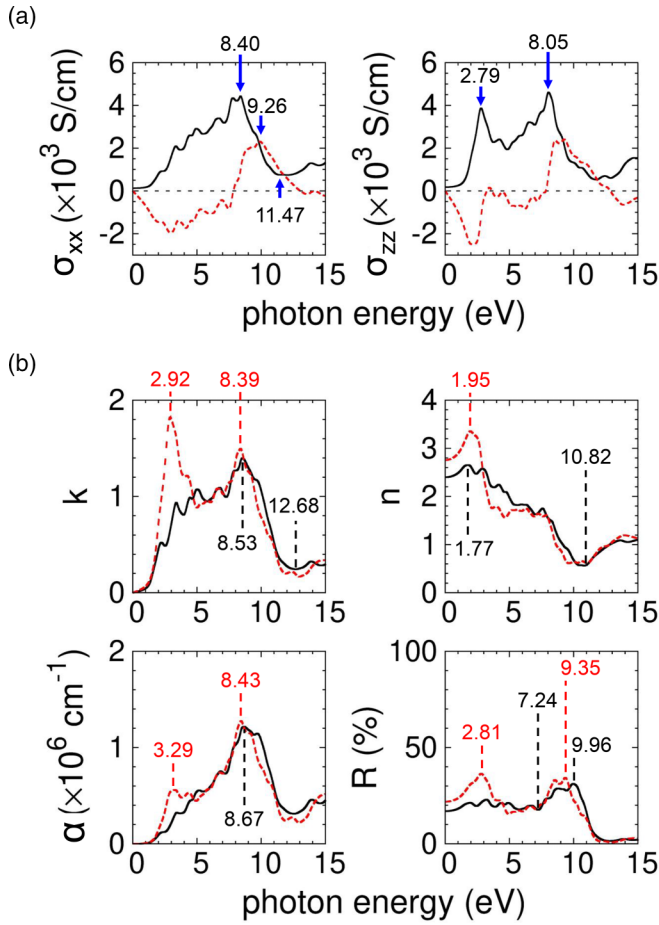
FIG. 5. (a) The optical conductivity of bulk Ca_2N. The black (red) lines indicate the real (imaginary) part of the optical conductivity. (b) Linear optical spectra of bulk Ca_2N. The black (red) lines indicate the linear optical spectra calculated from σ_{xx} (σ_{zz}). The unit of the numbers with the dashed lines is eV.

$$n(\omega) = \left(\frac{\sqrt{\mathrm{Re}(\varepsilon)^2 + \mathrm{Im}(\varepsilon)^2} + \mathrm{Re}(\varepsilon)}{2} \right)^{\frac{1}{2}}, \qquad (5)$$

$$R(\omega) = \frac{(n-1)^2 + k^2}{(n+1)^2 + k^2}, \qquad (6)$$

where α, k, n, and R indicate the absorption coefficient, extinction coefficient, refractive index, and reflectivity, respectively. The linear optical spectra for σ_{xx} and σ_{zz} are shown in Fig. 5(b). The black and red lines correspond to σ_{xx} and σ_{zz}, respectively. The vertical dashed lines indicate the peaks and dip positions of the linear optical spectra. The absorption coefficient α and extinction coefficient k are related to the real part of the optical conductivity $\sigma(\omega)$. The peaks of σ_{xx} occur in the ultraviolet (UV) region, while those of σ_{zz} occur in both the visible and UV regions. Therefore, the absorption coefficient α and extinction coefficient k have different peaks depending on whether they are perpendicular or parallel to the c axis.

The optical spectra of bulk Ca_2N suggest that it is a promising material for optoelectronic applications. The peaks in the optical conductivity indicate the presence of electronic transitions in the material, which can be used to absorb and emit light. This is essential for optoelectronic devices such as lasers and solar cells. The different peaks in the absorption coefficient for σ_{xx} and σ_{zz} suggest that bulk Ca_2N can be used to create polarization-sensitive devices. These devices can be used to filter light or to detect the polarization of light. Overall, the optical spectra of bulk Ca_2N provide valuable insights into the potential applications of this material in optoelectronics.

We investigated the absorption and extinction coefficients of bulk Ca_2N in the visible and UV regions. We found that the absorption and extinction coefficients were close to zero below the visible light region (0.00–1.59 eV) but increased steadily in the visible light region (1.59–3.26 eV). The peak absorption coefficient α determined from σ_{xx} was 8.67 eV, decreasing rapidly above this energy level. The absorption coefficient α calculated from σ_{zz} showed two peaks at 3.29 and 8.43 eV. The small peak at 3.29 eV was in the UV region but could be measured in the visible light region since it was smeared between 2.9 and 3.29 eV. Our results are in agreement with a previous study [29].

The extinction coefficient k, calculated from σ_{xx}, peaked at 8.53 eV and decreased above this energy level. The extinction coefficient k calculated from σ_{zz} showed peaks at 2.92 and 8.39 eV. We analyzed the resistance anisotropy in optical conductivity by examining the absorption and extinction coefficients. Our findings demonstrate that bulk Ca_2N exhibits anisotropic resistance within the 2 to 5 eV range (near-UV and visible light regions) while displaying isotropy beyond 6 eV (far-UV region). Notably, the presence of distinct plasmon modes, akin to excitons in 2D transition metal dichalcogenide materials [45], is suggested by the two peaks observed in the extinction coefficient derived from σ_{zz}. The photon energy-induced anisotropy leads us to expect various optical properties in 2D electrides on heterostructures.

We investigated the refractive index and reflectivity of bulk Ca_2N in the visible and UV regions. The refractive index and reflectivity showed a different pattern from the absorption and extinction coefficients. The refractive index n determined from σ_{xx} showed a peak of 2.65 at 1.77 eV, and its dip position was 0.56 at 10.82 eV. The refractive index n, calculated from σ_{zz}, peaked at 3.36 at 1.95 eV. The reflectivity R, determined from σ_{xx}, showed a peak of 31% at 9.96 eV and a plateau of almost 20% from 0.0 to 7.24 eV. In contrast, the reflectivity R calculated from σ_{zz} showed two peaks at 2.81 and 9.35 eV. The peak was 36% in the visible region and 34% in the UV region. Therefore, the optical transmission of the bulk Ca_2N was over 60% from the infrared (IR) to the UV. The reflectivity R of the bulk Ca_2N was almost 0% above 10 eV, indicating that the transmission of the bulk Ca_2N was close to 100% in the high-UV region. Under 7 eV, the refractive index exhibits anisotropy, with the peak heights crossing depending on the orientation relative to the c axis at 3 eV. The refractive index derived from σ_{zz} demonstrates higher peaks below 3 eV (in the infrared and visible light regions), while the refractive index peaks from σ_{xx} surpass those from σ_{zz} between 3 and 7 eV. Notably, the reflectivity displays anisotropy near the peak observed at 2.81 eV. These anisotropic characteristics manifest in the near-ultraviolet range (2 to 5 eV) through absorption and extinction coefficients and in the infrared and
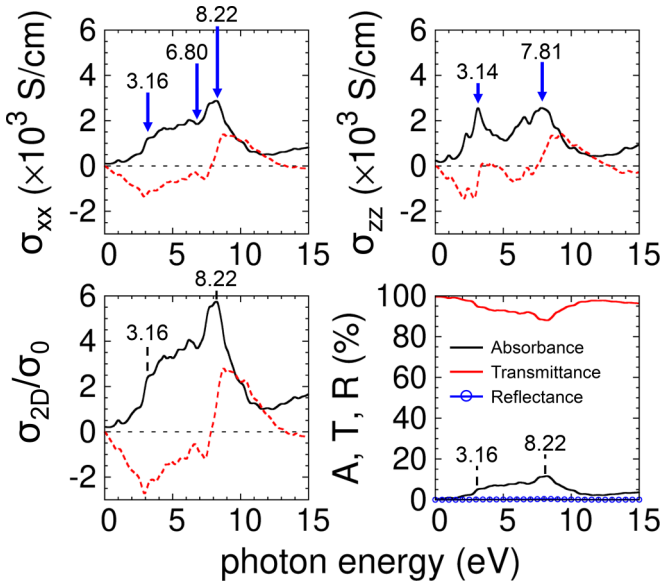
FIG. 6. Optical conductivity and optical spectra in the Ca_2N bilayer. The in-plane 2D optical conductivity is normalized by σ_0 [$= e^2/(4\hbar)$]. In optical conductivity plots, black lines represent the real part, and red lines represent the imaginary part. This distinction applies to both the overall optical conductivity and the specific in-plane 2D optical conductivity.

visible light regions (below 3 eV) through the refractive index and reflectivity measurements. When chemical adsorption occurs on the surface of Ca_2N, the reflectivity and refractive index peaks can differ depending on their orientation, whether parallel or perpendicular to the c axis.

Furthermore, we confirmed the linear optical properties of bilayer Ca_2N. We calculated the optical conductivity and plot it in Fig. 6. The in-plane optical conductivity σ_{xx} rapidly increases at 3.16 eV and plateaus between 3.16 and 6.80 eV. The highest peak appears at 8.22 eV. The out-of-plane optical conductivity σ_{zz} shows two peaks at 3.14 and 7.81 eV. The anisotropic characters in the near-UV range can be confirmed in the optical conductivity of the Ca_2N bilayer. However, the linear optical properties of 2D materials are influenced by the slab thickness of the materials; Eqs. (3)–(6) are ill defined in low-dimensional materials. Therefore, the optical conductivity $\sigma_{2D}(\omega)$ is considered for the optical properties of 2D sheets. The in-plane 2D optical conductivity $\sigma_{2D}(\omega)$ of bilayer Ca_2N is calculated as follows [46,47]:

$$\sigma_{2D}(\omega) = d\sigma_{xx}(\omega), \tag{7}$$

where d is the slab thickness. For bilayer Ca_2N, we set the slab thickness d to 12.15 Å, considering the covalent radius of Ca atoms. Based on the 2D optical conductivity, we can calculate the normalized conductivity $\tilde{\sigma}(\omega)$, reflectance $R(\omega)$, transmittance $T(\omega)$, and absorbance $A(\omega)$ as follows [46,47]:

$$\tilde{\sigma}(\omega) = \frac{\sigma_{2D}}{\varepsilon_0 c}, \tag{8}$$

$$R(\omega) = \left| \frac{\tilde{\sigma}/2}{1 + \tilde{\sigma}/2} \right|^2, \tag{9}$$

$$T(\omega) = \frac{1}{|1 + \tilde{\sigma}/2|^2}, \tag{10}$$

$$A(\omega) = \frac{\mathrm{Re}(\tilde{\sigma})}{|1 + \tilde{\sigma}/2|^2}, \tag{11}$$

where ε_0 and c are the vacuum permittivity and the speed of light, respectively. Moreover, R, T, and A were normalized such that $R + T + A = 1$. In this paper, we emphasize that the symbol R has two distinct meanings. In calculations for bulk, it refers to reflectivity, whereas in two-dimensional bilayers, it refers to reflectance. We plot the 2D optical conductivity and optical spectra in Fig. 6. Since the in-plane 2D optical conductivity σ_{2D} is calculated from the in-plane optical conductivity σ_{xx}, the peaks of σ_{2D} appear at the same photon energies as the peaks of σ_{xx}. Since the reflectance R is close to zero, the optical properties of the bilayer Ca_2N are dominated by the absorbance A. The transmittance T can be evaluated to $T \simeq 1 - A$. The absorbance shows a peak at 8.22 eV with a value of 11.58%. The absorbance plateaus between 3.16 and 6.80 eV, with values between 5% and 7%. This indicates that absorption is strongest in the far-UV region and weaker in the visible light range. The calculated transmittance is 88.01% at 8.22 eV and over 94.58% in the visible light range. These results show that bilayer Ca_2N has high transmission in the visible light region.

IV. CONCLUSIONS

In this study, we investigated the electronic and optical properties of Ca_2N, a 2D electride. We used DFT calculations with both PW and PAO basis sets. Our findings indicate that using PAO basis sets in DFT calculations without incorporating dummy atoms at the IAE and SAE sites leads to an incomplete representation of the electronic structures. To rectify this, we introduced dummy atoms at the IAE sites (in the bulk structure) and both IAE and SAE sites (in the bilayer structure), ensuring a more accurate description of the electronic structures. Additionally, we determined the optimal cutoff radius for the PAO basis sets by comparing the band structures obtained from PW and PAO calculations.

Our investigation also sheds light on the linear optical properties of bulk Ca_2N. We observed distinct peaks in the linear optical spectra of bulk Ca_2N, occurring in both the visible and UV regions, depending on the direction relative to the c axis (perpendicular or parallel). By calculating the dielectric functions from the band structures, we successfully elucidated the interband transitions involving the IAE and SAE states in both bulk and bilayer Ca_2N. Moreover, we propose that a deeper understanding of the IAE and SAE states can be attained through experimental measurements of the A_1 to A_2 ratio in the interband transitions of bulk Ca_2N.

The computational cost associated with PW basis set calculations for supercells with numerous atoms is substantial. Our results suggest that employing PAO basis sets in DFT calculations offers a promising approach to reduce computational expenses while still accurately describing the electronic structures of 2D electrides. Finally, we recommend that future investigations focus on exploring the nanoribbon structures of 2D electrides, as they exhibit distinct electronic and thermal transport properties compared to those of the 2D infinite layer.

[1] J. L. Dye, M. J. Wagner, G. Overney, R. H. Huang, T. F. Nagy, and D. Tománek, J. Am. Chem. Soc. **118**, 7329 (1996).

[2] J. L. Dye, Science **301**, 607 (2003).

[3] J. L. Dye, Science **247**, 663 (1990).

[4] J. L. Dye, Acc. Chem. Res. **42**, 1564 (2009).

[5] T. Tada, S. Takemoto, S. Matsuishi, and H. Hosono, Inorg. Chem. **53**, 10347 (2014).

[6] K. Lee, S. W. Kim, Y. Toda, S. Matsuishi, and H. Hosono, Nature (London) **494**, 336 (2013).

[7] J. Park, K. Lee, S. Y. Lee, C. N. Nandadasa, S. Kim, K. H. Lee, Y. H. Lee, H. Hosono, S.-G. Kim, and S. W. Kim, J. Am. Chem. Soc. **139**, 615 (2017).

[8] H. Huang, K.-H. Jin, S. Zhang, and F. Liu, Nano Lett. **18**, 1972 (2018).

[9] M. Hirayama, S. Matsuishi, H. Hosono, and S. Murakami, Phys. Rev. X **8**, 031067 (2018).

[10] S. Matsuishi, Y. Toda, M. Miyakawa, K. Hayashi, T. Kamiya, M. Hirano, I. Tanaka, and H. Hosono, Science **301**, 626 (2003).

[11] S. W. Kim, K. Hayashi, M. Hirano, H. Hosono, and I. Tanaka, J. Am. Ceram. Soc. **89**, 3294 (2006).

[12] S. W. Kim, S. Matsuishi, T. Nomura, Y. Kubota, M. Takata, K. Hayashi, T. Kamiya, M. Hirano, and H. Hosono, Nano Lett. **7**, 1138 (2007).

[13] M. Miyakawa, S. W. Kim, M. Hirano, Y. Kohama, H. Kawaji, T. Atake, H. Ikegami, K. Kono, and H. Hosono, J. Am. Chem. Soc. **129**, 7270 (2007).

[14] H. Hosono, S. W. Kim, S. Matsuishi, S. Tanaka, A. Miyake, T. Kagayama, and K. Shimizu, Philos. Trans. R. Soc. A **373**, 20140450 (2015).

[15] B. Cockayne and B. Lent, J. Cryst. Growth **46**, 467 (1979).

[16] M. G. DaGue, J. Landers, H. L. Lewis, and J. L. Dye, Chem. Phys. Lett. **66**, 169 (1979).

[17] M. Lacerda, J. T. S. Irvine, F. P. Glasser, and A. R. West, Nature (London) **332**, 525 (1988).

[18] P. Cauliez, J. Jackson, and J. Dye, Tetrahedron Lett. **32**, 5039 (1991).

[19] K. Hayashi, S. Matsuishi, T. Kamiya, M. Hirano, and H. Hosono, Nature (London) **419**, 462 (2002).

[20] W. Meng, X. Zhang, Y. Liu, X. Dai, G. Liu, Y. Gu, E. P. Kenny, and L. Kou, Adv. Sci. **10**, 2205940 (2023).

[21] X. Zhang, Z. Xiao, H. Lei, Y. Toda, S. Matsuishi, T. Kamiya, S. Ueda, and H. Hosono, Chem. Mater. **26**, 6638 (2014).

[22] S. Y. Lee, J.-Y. Hwang, J. Park, C. N. Nandadasa, Y. Kim, J. Bang, K. Lee, K. H. Lee, Y. Zhang, Y. Ma, H. Hosono, Y. H. Lee, S.-G. Kim, and S. W. Kim, Nat. Commun. **11**, 1526 (2020).

[23] L. M. McRae, R. C. Radomsky, J. T. Pawlik, D. L. Druffel, J. D. Sundberg, M. G. Lanetti, C. L. Donley, K. L. White, and S. C. Warren, J. Am. Chem. Soc. **144**, 10862 (2022).

[24] K. Horiba, R. Yukawa, T. Mitsuhashi, M. Kitamura, T. Inoshita, N. Hamada, S. Otani, N. Ohashi, S. Maki, J.-I. Yamaura, H. Hosono, Y. Murakami, and H. Kumigashira, Phys. Rev. B **96**, 045101 (2017).

[25] M. C. Barry, Z. Yan, M. Yoon, S. R. Kalidindi, and S. Kumar, Appl. Phys. Lett. **113**, 131902 (2018).

[26] D. Y. Novoselov, D. M. Korotin, A. O. Shorikov, V. I. Anisimov, and A. R. Oganov, J. Phys. Chem. C **125**, 15724 (2021).

[27] S. Kim, J. Bang, C. Y. Lim, S. Y. Lee, J. Hyun, G. Lee, Y. Lee, J. D. Denlinger, S. Huh, C. Kim, S. Y. Song, J. Seo, D. Thapa, S. G. Kim, Y. H. Lee, Y. Kim, and S. W. Kim, Nat. Mater. **21**, 1269 (2022).

[28] S. Guan, S. A. Yang, L. Zhu, J. Hu, and Y. Yao, Sci. Rep. **5**, 12285 (2015).

[29] D. L. Druffel, K. L. Kuntz, A. H. Woomer, F. M. Alcorn, J. Hu, C. L. Donley, and S. C. Warren, J. Am. Chem. Soc. **138**, 16089 (2016).

[30] P. Cudazzo and M. Gatti, Phys. Rev. B **96**, 125131 (2017).

[31] T. Ozaki, Phys. Rev. B **67**, 155108 (2003).

[32] G. Kresse and J. Hafner, Phys. Rev. B **47**, 558 (1993).

[33] G. Kresse and J. Furthmüller, Phys. Rev. B **54**, 11169 (1996).

[34] D. R. Hamann, M. Schlüter, and C. Chiang, Phys. Rev. Lett. **43**, 1494 (1979).

[35] L. Kleinman and D. M. Bylander, Phys. Rev. Lett. **48**, 1425 (1982).

[36] G. Kresse and D. Joubert, Phys. Rev. B **59**, 1758 (1999).

[37] D. Hobbs, G. Kresse, and J. Hafner, Phys. Rev. B **62**, 11556 (2000).

[38] J. P. Perdew, K. Burke, and M. Ernzerhof, Phys. Rev. Lett. **77**, 3865 (1996).

[39] S. Grimme, J. Antony, S. Ehrlich, and H. Krieg, J. Chem. Phys. **132**, 154104 (2010).

[40] J. Chae and G. Kim, Appl. Surf. Sci. **612**, 155721 (2023).

[41] W. Zou, K. Khan, X. Zhao, C. Zhu, J. Huang, J. Li, Y. Yang, and W. Song, Mater. Res. Express **4**, 036408 (2017).

[42] S. Matsuishi, S. W. Kim, T. Kamiya, M. Hirano, and H. Hosono, J. Phys. Chem. C **112**, 4753 (2008).

[43] K. Khan, A. K. Tareen, U. Khan, A. Nairan, S. Elshahat, N. Muhammad, M. Saeed, A. Yadav, L. Bibbó, and Z. Ouyang, Sci. Rep. **9**, 4967 (2019).

[44] M. Fox, *Optical Properties of Solids*, Oxford Master Series in Physics (Oxford University Press, Oxford, 2002).

[45] S. Huang, C. Song, G. Zhang, and H. Yan, Nanophotonics **6**, 1191 (2017).

[46] L. Matthes, O. Pulci, and F. Bechstedt, New J. Phys. **16**, 105007 (2014).

[47] L. Matthes, O. Pulci, and F. Bechstedt, Phys. Rev. B **94**, 205408 (2016)